Rotation of the asymptotic giant branch star R Doradus

Citation for the original published paper (version of record):
Vlemmings, W., Khouri, T., De Beck, E. et al (2018). Rotation of the asymptotic giant branch star R Doradus. Astronomy and Astrophysics, 613. http://dx.doi.org/10.1051/0004-6361/201832929

A&A 613, L4 (2018)
https://doi.org/10.1051/0004-6361/201832929

Astronomy & Astrophysics

LETTER TO THE EDITOR

Rotation of the asymptotic giant branch star R Doradus

W. H. T. Vlemmings[1], T. Khouri[1], E. De Beck[1], H. Olofsson[1], G. García-Segura[2], E. Villaver[3], A. Baudry[4], E. M. L. Humphreys[5], M. Maercker[1], and S. Ramstedt[6]

[1] Department of Space, Earth and Environment, Chalmers University of Technology, Onsala Space Observatory, 439 92 Onsala, Sweden
e-mail: `wouter.vlemmings@chalmers.se`
[2] Instituto de Astronomía, Universidad Nacional Autónoma de México, Km. 107 Carr. Tijuana-Ensenada, 22860 Ensenada B. C., Mexico
[3] Departamento de Física Teórica, Universidad Autónoma de Madrid, Cantoblanco, 28049 Madrid, Spain
[4] Laboratoire d'astrophysique de Bordeaux, Univ. Bordeaux, CNRS, B18N, Allée Geoffroy Saint-Hilaire, 33615 Pessac, France
[5] European Southern Observatory, Karl-Schwarzschild-Str. 2, 85748 Garching, Germany
[6] Department of Physics and Astronomy, Uppsala University, Box 516, 751 20 Uppsala, Sweden

Received 1 March 2018 / Accepted 12 April 2018

ABSTRACT

High-resolution observations of the extended atmospheres of asymptotic giant branch (AGB) stars can now directly be compared to the theories that describe stellar mass loss. Using Atacama Large Millimeter/submillimeter Array (ALMA) high angular resolution (30×42 mas) observations, we have for the first time resolved stellar rotation of an AGB star, R Dor. We measure an angular rotation velocity of $\omega_R \sin i = (3.5 \pm 0.3) \times 10^{-9}$ rad s^{-1}, which indicates a rotational velocity of $|\upsilon_{\rm rot} \sin i| = 1.0 \pm 0.1$ km s^{-1} at the stellar surface ($R_* = 31.2$ mas at 214 GHz). The rotation axis projected on the plane of the sky has a position angle $\Phi = 7 \pm 6°$. We find that the rotation of R Dor is two orders of magnitude faster than expected for a solitary AGB star that will have lost most of its angular momentum. Its rotational velocity is consistent with angular momentum transfer from a close companion. As a companion has not been directly detected, we suggest R Dor has a low-mass, close-in companion. The rotational velocity approaches the critical velocity, set by the local sound speed in the extended envelope, and is thus expected to affect the mass-loss characteristics of R Dor.

Key words. stars: AGB and post-AGB – stars: rotation

1. Introduction

Rotation of thermally pulsing (TP) asymptotic giant branch (AGB) stars can have significant effects on their interior structure and evolution. The internal dynamics is changed for example by the transport of angular momentum and turbulent mixing, and rotation-induced instabilities and rotational mixing can affect the nucleosynthesis and change relative stellar yields (e.g. Lagarde et al. 2012; Piersanti et al. 2013). Differential rotation can also generate strong magnetic fields (e.g. Blackman et al. 2001). Finally, rotation can directly affect the mass loss by changing the isotropic wind into one with a strong equatorial component (e.g. Dorfi & Hoefner 1996; Ignace et al. 1996).

Stellar evolution models predict surface rotation velocities for (solitary) low- to intermediate-mass TP-AGB stars of only a few 10 s of m s^{-1}. As far as we know, the carbon AGB star V Hya is the only AGB star for which fast rotation has been inferred from spectroscopic observations (Barnbaum et al. 1995). As V Hya also displays evidence of a high-velocity collimated outflow with multiple components, it has been suggested that V Hya is a late-AGB star in a binary system (e.g. Sahai et al. 2016). Here we present the first direct detection of rotation of the extended atmosphere of an AGB star, R Dor. R Dor is a nearby (59 pc; Knapp et al. 2003) M-type AGB star with a slow wind and a low mass-loss rate ($\upsilon_{\rm exp} = 5.7$ km s^{-1}, $\dot{M} = 1{-}2 \times 10^{-7}$ $M_\odot$ yr^{-1}; Ramstedt & Olofsson 2014; Maercker et al. 2016). Based on the oxygen isotopologue ratios Si^{17}O/Si^{18}O and H$_2^{17}$O/H$_2^{18}$O as proxies for the isotopic ratio ^{17}O/^{18}O, the initial stellar mass of R Dor is estimated to be 1.3−1.6 $M_\odot$ (De Beck & Olofsson 2018; Danilovich et al. 2017).

2. Observations and data reduction

These observations of R Dor were performed as part of ALMA project 2016.1.0004.S. Here we mainly focus on observations in Band 6, although Band 4 observations confirm the results. The observations took place on 25 September 2017 and were performed using four spectral windows (spws) of 1920 channels each. The velocity resolution was ~1.4 km s^{-1} and the spws were centred on 213.97, 215.97, 226.29, and 228.21 GHz. Further details of the calibration and self-calibration will be presented in a forthcoming paper (Vlemmings et al., in prep.).

The stellar continuum emission of R Dor is clearly detected and resolved. Using the uv-fitting procedure decribed in Vlemmings et al. (2017), we have determined the size of R Dor at 214 GHz to be $(62.4 \pm 0.1) \times (61.8 \pm 0.1)$ mas at a position angle of $33 \pm 6°$ east from north. The continuum emission was subtracted before the subsequent line imaging. The line image products were created using Briggs robust weighting. This resulted in a typical beam size of 30×42 mas and a typical channel rms noise of ~2.5 mJy beam^{-1}. Since the data were taken in one of the longest baseline configurations, the maximum

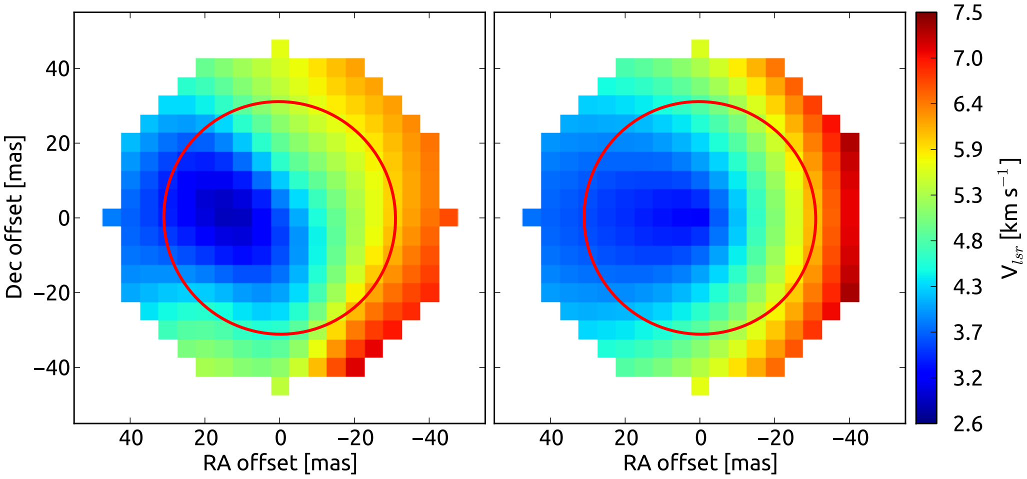

Fig. 1. *Left*: Centre velocity of the SiO $v = 3, J = 5-4$ emission line as determined from a fit to the observations. In this and the other panels, the red ellipse indicates the measured size of the star at 214 GHz. *Right*: Best-fit model of solid-body rotation (see text).

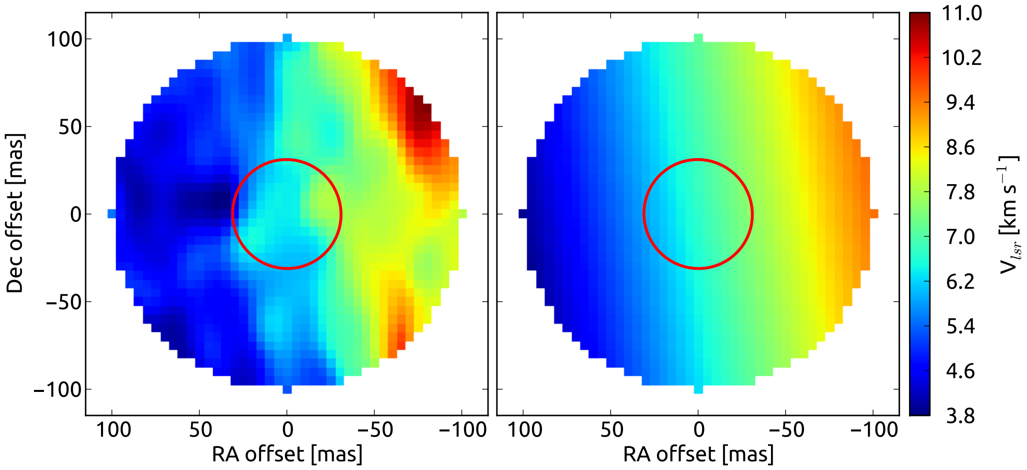

Fig. 2. Same as Fig.1 for the SO_2 $J_{K_a,K_c} = 16_{3,13} - 16_{2,14}$ line.

recoverable scale is $\sim$0.35″. Hence we are mainly sensitive to strong compact emission.

3. Results

Numerous molecular lines were detected towards R Dor. Here we focus mainly on two of the SiO lines and an SO_2 line, namely the SiO $v = 3, J = 5-4$ and SO_2 $J_{K_a,K_c} = 16_{3,13} - 16_{2,14}$ emission lines and the ^{29}SiO $v = 1, J = 5-4$ absorption line. Hereafter, we denote the lines as SiO $v = 3$, SO_2, and ^{29}SiO $v = 1$. The lines are compact and detected at sufficiently high signal-to-noise ratio to allow a careful analysis of their velocity structure within three stellar radii. Additionally, although some maser action might be present in the strongest emission peak of the SiO $v = 3$ line, its line width and strength do not indicate a strong masing effect. Any further discussion on the line emission and absorption characteristics and excitation is beyond the scope of this Letter.

As the lines in the stellar atmosphere are affected by pulsations and convective motions, the line widths are large. We measure widths of $\sim$5–10 km s^{-1} for the SO_2 line , $\sim$10 km s^{-1} for the SiO $v = 3$ line, and $\sim$15–20 km s^{-1} for the ^{29}SiO $v = 1$ line. In order to describe the velocity field around the star, we fit the spectra from each image pixel using the CASA task *specfit*. In Fig. A.1 we present the line spectra for the SiO $v = 3$, SO_2, and ^{29}SiO $v = 1$ lines, taken in an aperture covering the dominant part of the line emission region, and the resulting fit and residual spectra. We found that a single Lorentzian profile accurately describes the majority of the spectral lines, although the strong absorption line of ^{29}SiO $v = 1$ is better fitted with two Gaussian components. The fitting task produces images of intensity, central velocity, full-width at half-maximum (FWHM) line width and their respective errors. For the SiO $v = 3$ and SO_2 lines, they and the fit residuals are shown in Figs. 1, A.2, A.3, and Figs. 2, A.4, A.5, respectively. The velocity field of the strongest ^{29}SiO $v = 1$ component is presented in Fig. A.6, and its residual, error, intensity, and FWHM maps are shown in Figs. A.7 and A.8. Because this line was seen only in absorption against the star and hence is only marginally resolved, we base our main results on the two other lines. Channel maps for the three lines discussed here are shown in Appendix B.

The velocity field of the three lines presented here all show a clear gradient across the entire emitting region from red-shifted to blue-shifted velocities with respect to the systemic velocity. Generally, velocity gradients could be caused by an outflow, an expanding and/or rotating disc or torus, rotation of the entire emitting structure, or a chance alignment of convective cells producing outward motions. Since we see the velocity gradients out to at least two R_*, we can rule out a chance alignment of convective cells. At the outflow velocities measured, material would have to be coherently ejected from above convective cells for a period of more than two years to produce the observed distribution. This is longer than typical convective timescales (Freytag et al. 2017).

Based on the line intensity distributions, we can also rule out an edge-on torus or disc since there is no sign of a flattened distribution across the star. Furthermore, as we observe the rotation within 1.1 R_*, its origin in a disc or torus means that this structure would have to extend to the surface of the star, without any gap. This is in contrast to a recent tentative claim of an edge on disc, with an inner radius of ~6 au, around R Dor by Homan et al. (2018). They report a velocity gradient, fully consistent with our interpretation of solid-body rotation, observed in different molecular lines but with significantly lower angular resolution (~150 mas). Because of the lack of resolution, the authors suggested a disc. Their tentative interpretation is not consistent with the data presented here. Moreover, observations of dust-scattered light between 2 and 10 R_* do not support the idea of an edge-on disc (Khouri et al. 2016, and in prep.).

A tilted expanding disc or torus seen almost face-on could explain the velocities seen in the SO_2 and other extended lines. It would not produce the pattern of red- to blue-shifted velocities seen in the SiO lines across the stellar disc, however. Similarly, a bipolar outflow would not produce such a pattern across the stellar disc unless the outflow has an opening angle close to 180° and material is launched almost tangentially to the surface near the equator. There is no known mechanism that would explain such an outflow originating at the stellar surface. Consequently, we conclude that only rotation of the star and its envelope can explain the velocity field that is observed.

The velocity field was fit using a χ^2-analysis to the velocity field produced by the rotation of a shell with solid-body rotation. The rotation velocity for solid-body rotation including possible expansion is given by (e.g. Kervella et al. 2018)

$$\upsilon_{\rm obs}(p) = \frac{p_y}{R_{\rm shell}}(\upsilon_{\rm rot}\sin i) + \left(\upsilon_{\rm sys} - \upsilon_{\rm exp}\frac{(R_{\rm shell}-p)}{R_{\rm shell}}\right). \quad (1)$$

Here, $\upsilon_{\rm obs}$ is the observed velocity, p is the projected distance on the sky from the centre of the star, and p_y is the component of p perpendicular to the rotation axis (with position angle Φ). $R_{\rm shell}$ is the average shell radius of the emission line, $\upsilon_{\rm rot}$ is the rotation velocity at $R_{\rm shell}$, and i is the unknown inclination of the rotation axis. Additional velocity components correspond to the systemic velocity $\upsilon_{\rm sys}$ of the line and the expansion velocity $\upsilon_{\rm exp}$ ($\upsilon_{\rm exp} = 0$ for $p > R_{\rm shell}$). As noted in Kervella et al. (2018), there is a strong correlation between $\upsilon_{\rm sys}$ and $\upsilon_{\rm exp}$ if the observations provide only a few resolution elements across the emission region, which is the case for our observations. We determined for the emission lines the average shell radius $R_{\rm shell}$ using *immultifit* (Martí-Vidal et al. 2014) by fitting a shell of emission to each individual channel. We then took $R_{\rm shell}$ to be the weighted average of the four central emission channels. Finally, the χ^2 analysis was performed using the maps of pixel-based central velocity and the associated errors produced using *specfit*. We limited the pixels we included to those where the fitted amplitudes were at least three times the associated fit error. The results of the fits are presented in Table 1 and are shown with the measured velocity fields in Figs. 1, 2, and A.6. The velocity error map, used in the χ^2 analysis, and the residual velocity maps are shown in the same figures. The amplitude and line-width maps for the same lines are shown in Appendix B. Although the approximation of solid-body rotation for each individual molecular line might not be fully correct, our angular resolution does not allow us to fit the extra parameters needed for a more detailed description of the rotation. However, a comparison between the SiO $\upsilon = 3$ and SO_2 lines that peak at significantly different radii yields results for the angular rotation velocity that are consistent within $<1.5\sigma$. We thus conclude that the extended atmosphere indeed appears to display solid-body rotation out to at least two R_* and adopt from a weighted average of the SiO $\upsilon = 3$ and SO_2 lines an angular rotation velocity of $\omega_R \sin i = (3.5 \pm 0.3) \times 10^{-9}$ rad s^{-1} for the stellar atmosphere of R Dor. This implies a rotation period $P/\sin i = 57 \pm 5$ yr. The weighted average position angle of the rotation axis $\Phi = 7 \pm 6°$.

In addition to the lines emitting close to the star, we also detect a feature extending out to ~0.4″ (corresponding to $>10R_*$) at an anomalous velocity in a number of other lines. In our observations, this is most obvious in the ^{29}SiO $\upsilon = 0, J = 5 - 4$ line, for which we present a position-velocity diagram in Fig. 3. As indicated in this diagram, the velocity of this extended feature is consistent with the solid-body rotation that was determined in the other lines, out to a much larger distance. However, the feature is seen in the south-east at a position angle of ~135°, which would imply a position angle of the rotation axis of ~45°. If the position angle instead were ~7°, as determined from the other lines, the solid-body angular velocity of the feature would be $\sim 6.7 \times 10^{-9}$ rad s^{-1}. No corresponding feature is seen on the other side of R Dor.

4. Discussion

4.1. Origin of the rotation

Standard angular momentum conservation considerations imply that TP-AGB stars should be slow rotators. The actual surface rotation is affected by a variety of processes, such as mass loss and magnetic breaking, during stellar evolution. We compare our observations with a detailed model for a star with an initial mass of 1.5 $M_\odot$ and an initial rotation velocity of 50 km s^{-1}, which uses the same code and physics as explained in García-Segura et al. (2014). The velocity corresponds to a typical magnetically braked main-sequence rotation velocity for such a star (e.g. Calvet & Peimbert 1983). The velocity at which the centrifugal force balances gravity, in the absence of radiation pressure, is ~250 km s^{-1}, but the majority of stars rotate slower than 40% of this velocity on the main sequence (Huang et al. 2010). Once the star reaches the thermally pulsing AGB phase and reaches the measured temperature (~2100 K) and radius (≈400 $R_\odot$ at 59 pc), the surface rotation velocity has dropped to ~0.01 km s^{-1}. The rotation velocity remains of this order even when higher initial main-sequence rotational velocities are considered (García-Segura et al. 2014). This is at least two orders of magnitude lower than what we find. Unless the theory is incomplete, it is unlikely that the rotation we measure originates in the fast initial rotation of a single star.

García-Segura et al. (2016) determined stellar rotation in the presence of a companion. In these models, it is possible to achieve velocities similar to what we observe by invoking a companion within 8 au. For sub-stellar companions, we can also constrain the inner radius to be $\gtrsim$2.5 au considering that during the pre-AGB evolution, this region would be gravitationally cleared (Mustill & Villaver 2012). For illustration purpose, a 0.1 $M_\odot$ companion at 5 au on a circular orbit would have a total angular momentum $\sim 2 \times 10^{45}$ kg m^2 s^{-1}. This corresponds to approximately ten times the angular momentum estimated to be imparted to R Dor.

Thus, the most likely cause of the observed rotation is an as yet undetected low-mass companion. However, this does not explain the apparent solid-body rotation out to several stellar radii. Specifically, the origin of the fast-rotating feature out to >10 R_* remains unclear. If this feature is somehow related to

Table 1. Rotation model fit results.

Line	Rest freq. [GHz]	R_{shell} [mas]	$\upsilon_{R,\mathrm{rot}} \sin i$ [km s^{-1}]	$\omega_R \sin i$ [10^{-9} rad s^{-1}]	υ_{sys} [km s^{-1}]	υ_{exp} [km s^{-1}]	Φ [°]	χ^2_{red}
SiO $\upsilon = 3, J = 5-4$	212.5826	36 ± 1	-1.4 ± 0.3	4.7 ± 0.8	4.9 ± 0.2	1.7 ± 0.2	-1 ± 11	1.13
SO$_2$ $J_{K_{\mathrm{a}},K_{\mathrm{c}}} = 16_{3,13} - 16_{2,14}$	214.68939	66 ± 2	-1.8 ± 0.1	3.2 ± 0.2	6.7 ± 0.1	0.0 ± 0.1	9 ± 4	0.89
^{29}SiO $\upsilon = 1, J = 5-4^{a}$	212.90515	–	-4.1 ± 1.0^{b}	15 ± 4	3.1 ± 0.2	–	3 ± 16	1.46

Notes. [a] Only seen in absorption against the star. The fit represents the brightest of two absorption components. [b] The velocity at R_*.

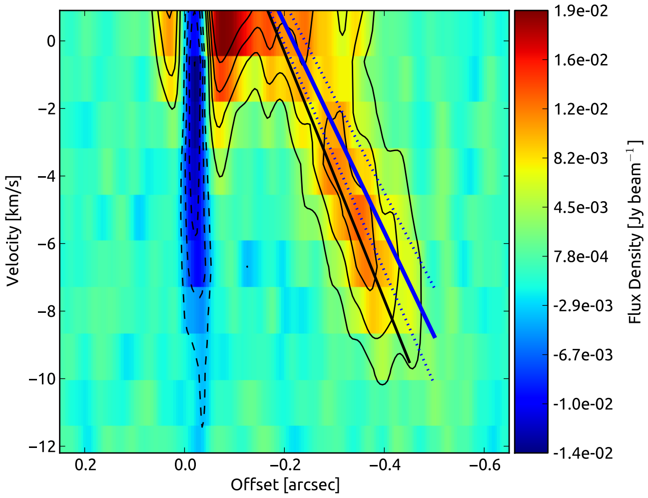

Fig. 3. Position-velocity diagram of the ^{29}SiO $\upsilon = 0, J = 5-4$ line at a rest frequency of 214.385741 GHz. The diagram is extracted along a slit through the star with a width of 0.1″ at a position angle of 135°. Contours are drawn at -16 to 16σ in steps of 4σ, where $\sigma = 0.9$ mJy beam^{-1}. We only show the blue-shifted channels to highlight the linear feature extending to ~0.4″. The offset is with respect to the star. The stellar velocity is 6.7 km s^{-1}. The blue lines indicates solid-body rotation with an angular velocity of $(3.5 \pm 0.3) \times 10^{-9}$ rad s^{-1} (for a position angle of the rotation axis of 45°, the dotted lines correspond to the quoted uncertainties). The black line corresponds to an angular velocity of 6.7×10^{-9} rad s^{-1} when assuming a position angle of the rotation axis of 7°. The absorption feature against the star is due to the dynamic stellar atmosphere.

the rotation, one might expect it to be found close to the equatorial plane. As the position angle of the feature is very different from that of the rotation axis, this would require a relatively small inclination i and hence an even higher rotation velocity, or a significant change of the rotation axis. Alternatively, this feature could be unrelated to the rotation and represent a seemingly one-sided ejection of material.

4.2. Effect of the rotation

The critical velocity for rotation that has an influence on the AGB atmospheric structure is set by the local sound speed (e.g. Ignace et al. 1996; García-Segura et al. 2014). For typical AGB atmospheres, this velocity ranges from ~5 km s^{-1} near the stellar photosphere to ~1 km s^{-1} farther out in the circumstellar envelope (CSE). Our measured velocity at ~2 R_* is similar to the local sound speed, assuming typical temperature and density, and would even exceed it if $i \lesssim 40°$. The rotation is thus expected to have a measurable effect on the density distribution through the CSE. Specifically, models predict a density contrast between the equatorial and polar regions exceeding a factor of three (Ignace et al. 1996; Dorfi & Hoefner 1996). No strong effect on the circumstellar environment of R Dor are immediately apparent. This could be consistent with a rotation axis inclination angle ≳45°, which would imply that we mainly see the equatorial region projected on the plane of the sky. Finally, we note that our measured angular rotation could be sufficient to sustain a rotational dynamo, although the magnetic field strength of R Dor is yet to be determined.

5. Conclusions

We presented the first direct observations of rotation of an AGB star other than the fast-rotating star V Hya, which is thought to be transitioning to the post-AGB stage (e.g. Sahai et al. 2016). We measure an apparent angular rotation velocity of the oxygen-rich AGB star R Dor of $\omega_R \sin i = 3.5 \pm 0.3 \times 10^{-9}$ rad s^{-1}, equivalent to a rotation velocity of $|\upsilon_{\mathrm{rot}} \sin i| = 1.0 \pm 0.1$ km s^{-1} at the observed (214 GHz) stellar radius of $R_* = 1.84$ au. The solid-body rotation appears to extend to at least 2 R_*, where we measure a rotation velocity $|\upsilon_{\mathrm{rot}} \sin i| \sim 1.8 \pm 0.1$ km s^{-1}.

Although the inclination of the rotation axis is currently unknown, the rotation velocity exceeds what can be produced by single-star evolution models by almost two orders of magnitude. This would suggest that R Dor has an unseen companion from which angular momentum is transferred to its extended atmosphere. No such companion has been directly detected. A study of the dust-scattered light in the dust formation zone of R Dor does not show obvious asymmetries due to an interaction either (Khouri et al. 2016, and in prep.). Furthermore, we are also not aware of any reported large-scale bipolar outflow or spiral structure that could be the result of binary interaction. Schöier et al. (2004) noted a ~ 1″-scale asymmetry in the SiO $\upsilon = 0, J = 2-1$ envelope.

Since R Dor is the nearest known AGB star, it should be possible to identify the nature of the companion. It will then be a prime candidate for observing close binary interaction in detail, and specifically, investigating binary and/or rotation effects on dust formation and the generation of AGB winds. As the rotation velocity approaches the local sound speed, the mass loss should no longer be fully isotropic. Hence R Dor might also be a progenitor of an a-spherical planetary nebula.

Acknowledgements. This work was supported by ERC consolidator grant 614264. WV, TK and HO acknowledge support from the Swedish Research Council. EDB acknowledges support from the Swedish National Space Board. This paper makes use of the following ALMA data: ADS/JAO.ALMA#2016.1.00004.S. ALMA is a partnership of ESO (representing its member states), NSF (USA) and NINS (Japan), together with NRC (Canada), NSC and ASIAA (Taiwan), and KASI (Republic of Korea), in cooperation with the Republic of Chile. The Joint ALMA Observatory is operated by ESO, AUI/NRAO and NAOJ.

References

Barnbaum, C., Morris, M., & Kahane, C. 1995, ApJ, 450, 862
Blackman, E. G., Frank, A., Markiel, J. A., Thomas, J. H., & Van Horn H. M. 2001, Nature, 409, 485
Calvet, N., & Peimbert, M. 1983, Rev. Mex. Astron. Astrofis., 5, 319
Danilovich, T., Lombaert, R., Decin, L., et al. 2017, A&A, 602, A14
De Beck, E. & Olofsson, H. 2018, A&A, in press, DOI: `10.1051/0004-6361/201732470`
Dorfi, E. A., & Hoefner, S. 1996, A&A, 313, 605
Freytag, B., Liljegren, S., & Höfner, S. 2017, A&A, 600, A137
García-Segura, G., Villaver, E., Langer, N., Yoon, S.-C., & Manchado, A. 2014, ApJ, 783, 74
García-Segura, G., Villaver, E., Manchado, A., Langer, N., & Yoon, S.-C. 2016, ApJ, 823, 142
Homan, W., Danilovich, T., Decin, L., et al. 2018, A&A, in press, DOI: `10.1051/0004-6361/201732246`
Huang, W., Gies, D. R., & McSwain, M. V. 2010, ApJ, 722, 605
Ignace, R., Cassinelli, J. P., & Bjorkman, J. E. 1996, ApJ, 459, 671
Kervella, P., Decin, L., Richards, A. M. S., et al. 2018, A&A, 609, A67
Khouri, T., Maercker, M., Waters, L. B. F. M., et al. 2016, A&A, 591, A70
Knapp, G. R., Pourbaix, D., Platais, I., & Jorissen, A. 2003, A&A, 403, 993
Lagarde, N., Decressin, T., Charbonnel, C., et al. 2012, A&A, 543, A108
Maercker, M., Danilovich, T., Olofsson, H., et al. 2016, A&A, 591, A44
Martí-Vidal, I., Vlemmings, W. H. T., Muller, S., & Casey, S. 2014, A&A, 563, A136
Mustill, A. J., & Villaver, E. 2012, ApJ, 761, 121
Piersanti, L., Cristallo, S., & Straniero, O. 2013, ApJ, 774, 98
Ramstedt, S., & Olofsson, H. 2014, A&A, 566, A145
Sahai, R., Scibelli, S., & Morris, M. R. 2016, ApJ, 827, 92
Schöier, F. L., Olofsson, H., Wong, T., Lindqvist, M., & Kerschbaum, F. 2004, A&A, 422, 651
Vlemmings, W., Khouri, T., O'Gorman, E., et al. 2017, Nat. Astron., 1, 848

Appendix A: Supplementary material

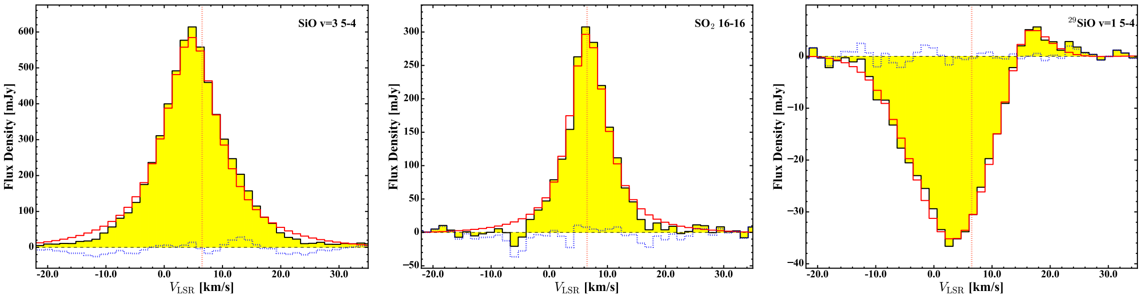

Fig. A.1. Total intensity spectrum of the ^{28}SiO $v = 3$, $J = 5-4$ *(left)* and the SO$_2$ $J_{K_a,K_c} = 16_{3,13} - 16_{2,14}$ *(middle)*, and the ^{29}SiO $v = 1, J = 5-4$ *(right)* transitions around R Dor. The spectra are extracted using a circular aperture with a diameter of 0.09″, 0.2″, and 0.075″ for the SiO $v = 3$, SO$_2$, and ^{29}SiO $v = 1$ lines, respectively. The observed spectra are shown in black. The best-fit CASA *specfit* model for each line is shown in red, while the residuals are indicated by the dashed blue histogram.

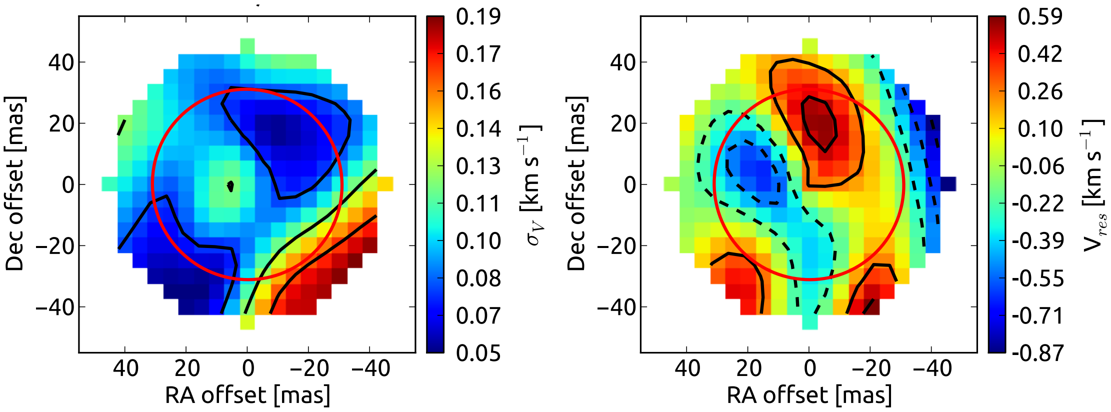

Fig. A.2. *Left*: velocity error map as derived from the pixel-based spectral fit of the SiO $v = 3, J = 5-4$ line, which we used in the χ^2 analysis. *Right*: velocity residual map.

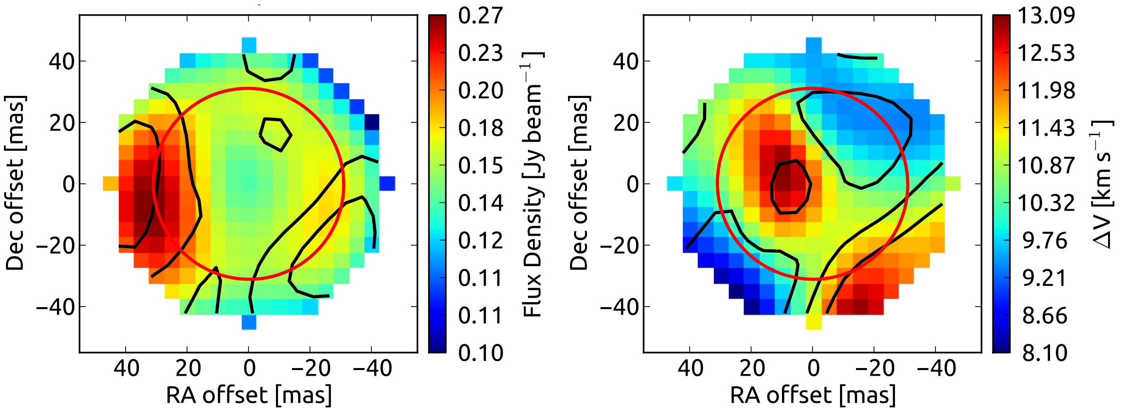

Fig. A.3. *Left*: intensity map of SiO $v = 3, J = 5-4$ as derived from the pixel-based spectral fit. The contours indicate the fitted rms errors at 2, 3, and 4 mJy beam^{-1}. *Right*: FWHM velocity map. The contours indicate the fitted rms errors at levels of 0.26, 0.39, and 0.52 km s^{-1}.

Here we present the spectra for the SiO $v = 3, J = 5-4$, SO$_2$ $J_{K_a,K_c} = 16_{3,13} - 16_{2,14}$, and ^{29}SiO $v = 1, J = 5-4$ lines. We also show the velocity map and model for the ^{29}SiO $v = 1$, J=5-4 line as well as the error, residual, intensity, and FWHM velocity maps produced by *specfit* for the SiO $v = 3, J = 5-4$, SO$_2$ $J_{K_a,K_c} = 16_{3,13} - 16_{2,14}$, and ^{29}SiO $v = 1, J = 5-4$ lines.

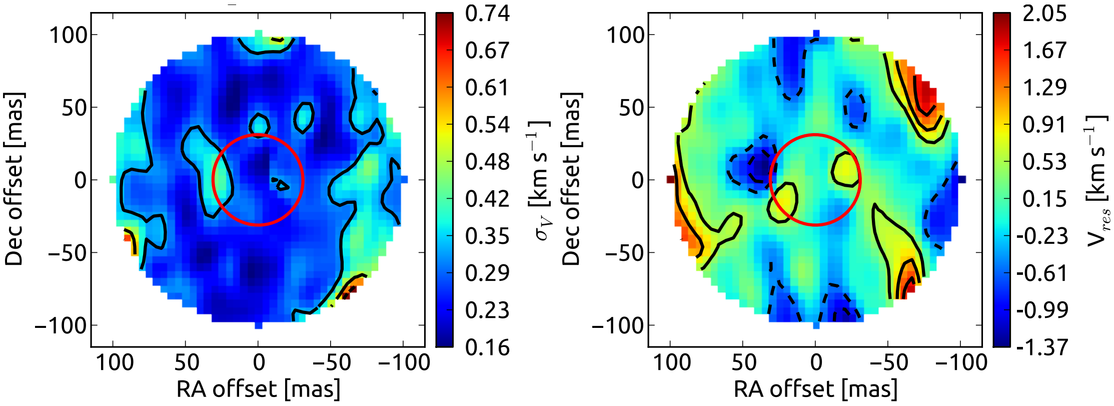

Fig. A.4. Same as Fig.A.2 for the SO$_2$ $J_{K_a,K_c} = 16_{3,13} - 16_{2,14}$ line.

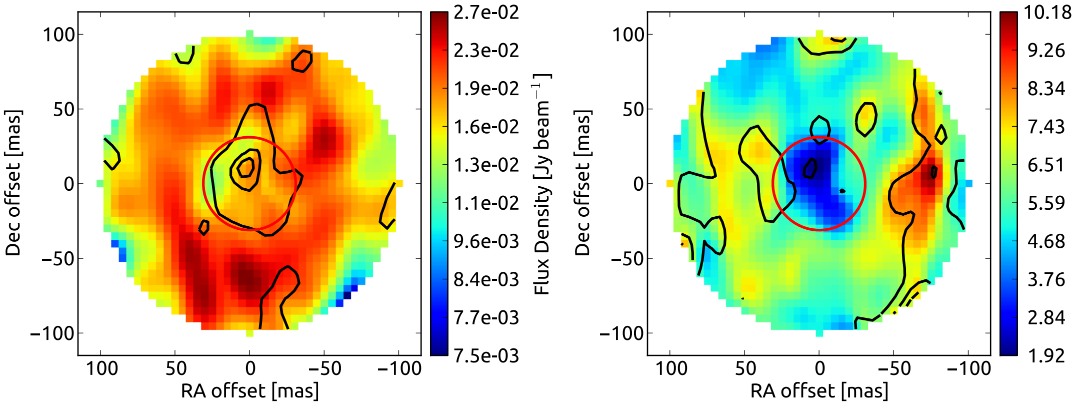

Fig. A.5. Same as Fig.A.3 for the SO$_2$ $J_{K_a,K_c} = 16_{3,13} - 16_{2,14}$ line. The fitted intensity errors are plotted at 2, 4, and 6 mJy beam^{-1}. The fitted FWHM velocity errors are plotted at 1.0, 1.5, and 2.0 km s^{-1}.

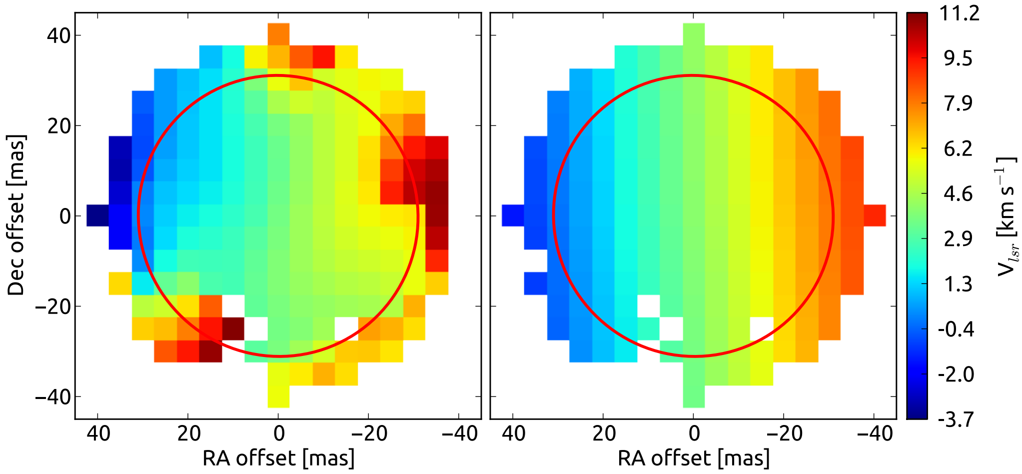

Fig. A.6. Same as Fig. 1 for the dominant absorption component of the ^{29}SiO $\upsilon = 1, J = 5 - 4$ line.

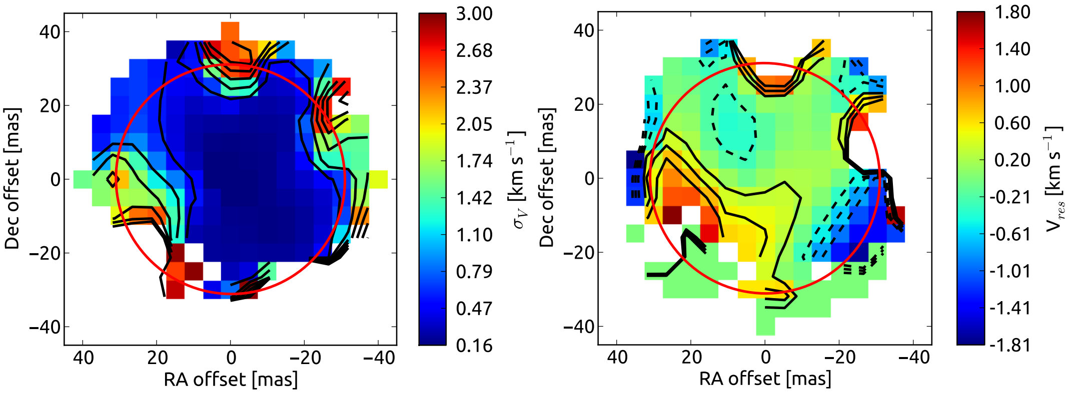

Fig. A.7. Same as Fig. A.2 for the dominant absorption component of the ^{29}SiO $v = 1, J = 5 - 4$ line.

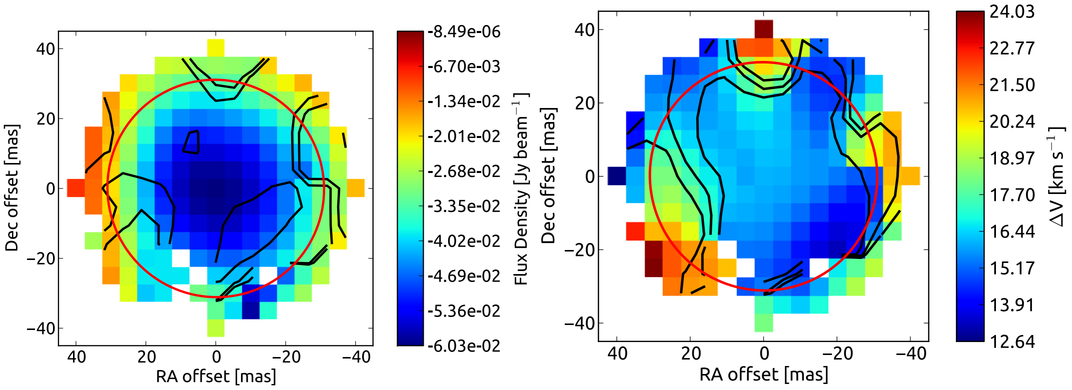

Fig. A.8. Same as Fig. A.3 for the dominant absorption component of the ^{29}SiO $v = 1, J = 5 - 4$ line. The fitted intensity errors are plotted at 1, 2, and 4 mJy beam^{-1}. The fitted FWHM velocity errors are plotted at 1.0, 1.5, and 2.0 km s^{-1}.

Appendix B: Channel maps

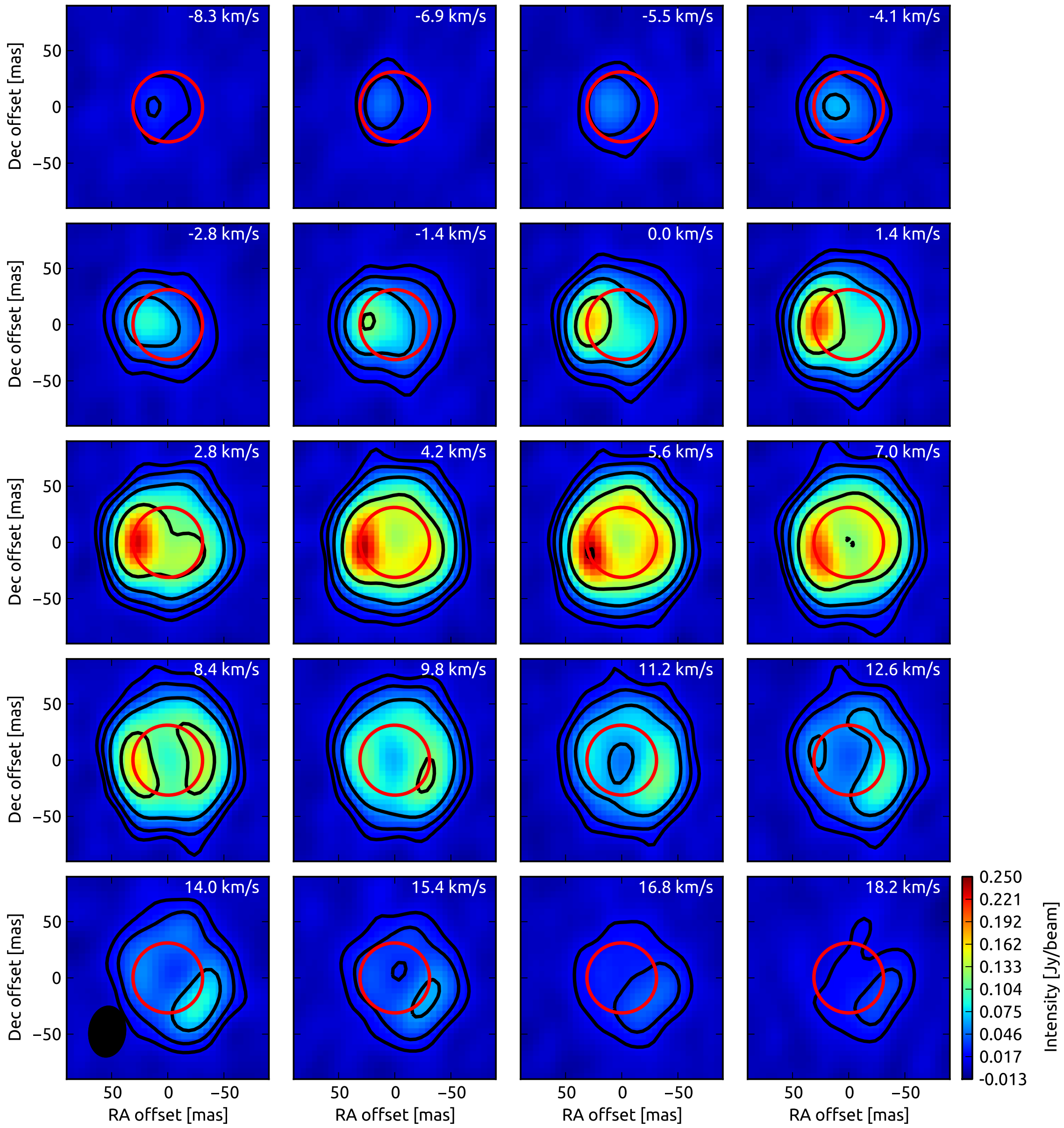

Fig. B.1. Channel maps for the SiO $v = 3, J = 5-4$ emission line. The red ellipse denotes the size of the measured stellar disc. Contours are drawn at $6, 12, 24, 48,$ and 96σ with $\sigma = 2.5$ mJy beam^{-1}. The beam size is indicated in the *bottom left panel*.

Here we present the channel maps for the SiO $v = 3, J = 5-4$, SO$_2$ $J_{K_a,K_c} = 16_{3,13} - 16_{2,14}$, and ^{29}SiO $v = 1, J = 5-4$ lines.

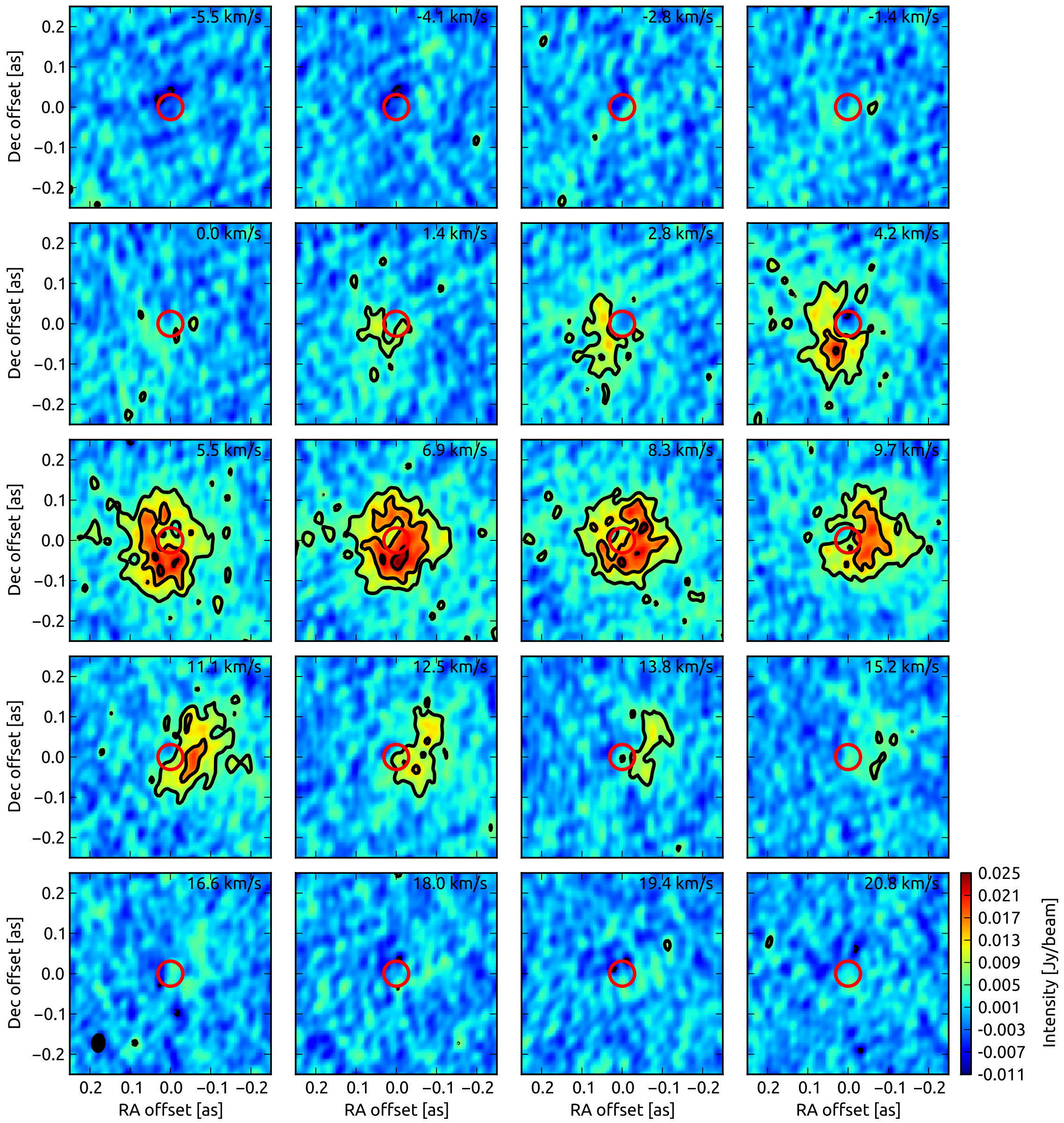

Fig. B.2. Same as Fig. B.1 for the SO_2 $J_{K_a,K_c} = 16_{3,13} - 16_{2,14}$ emission line. Contours are drawn at 3, 6, 9, and 12σ with $\sigma = 2.5$ mJy beam^{-1}.

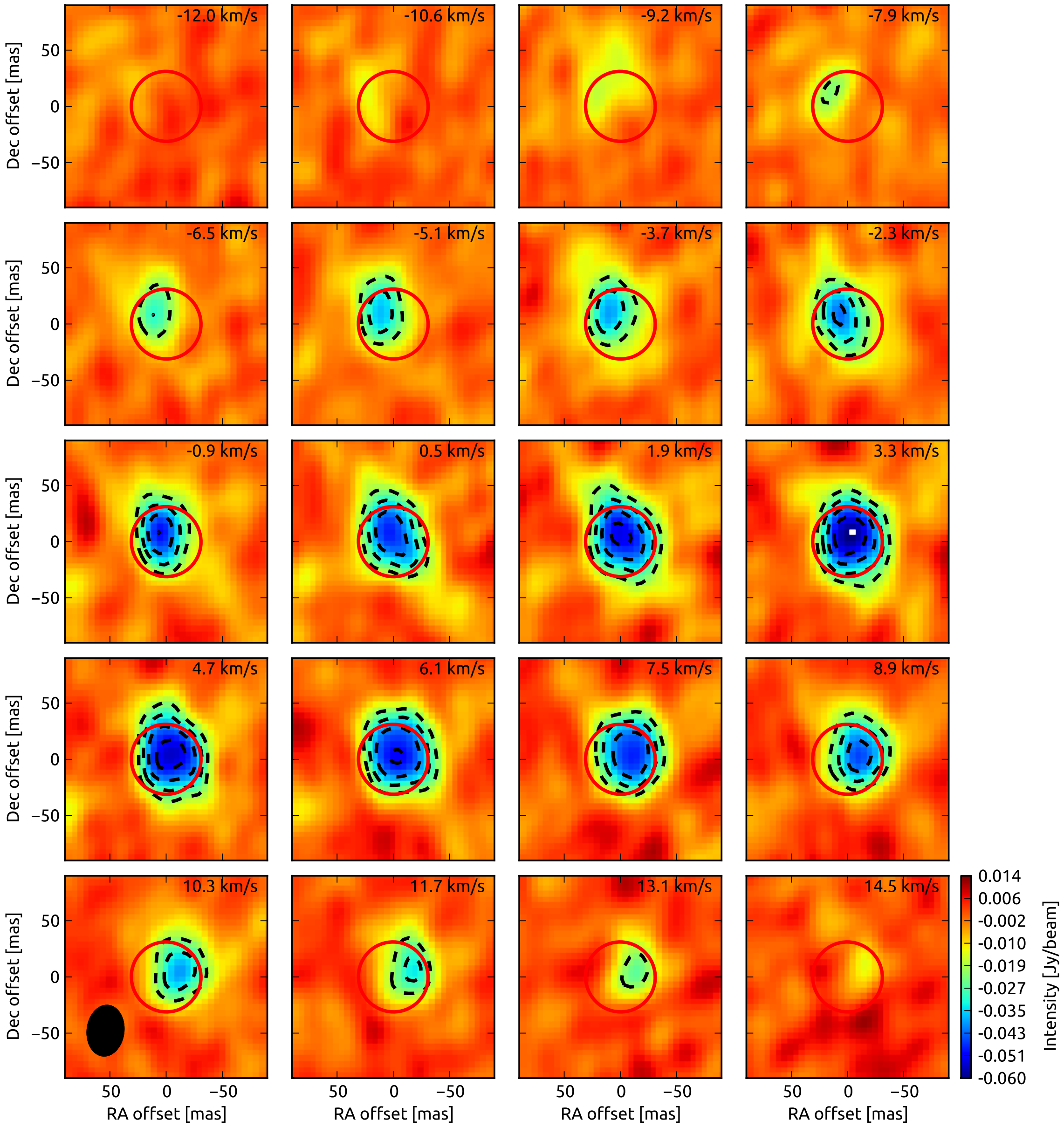

Fig. B.3. Same as Fig. B.1 for the ^{29}SiO $v = 1, J = 5-4$ line seen in absorption. Contours are drawn at $-16, -12$, and -8σ with $\sigma = 2.5$ mJy beam^{-1}.